Analytical Optimization of Polarimetric Change Detectors for Mapping Open and Grassland Flooding Using Sentinel-1. Case of Rupununi, Guyana

Felix Kasiti Isundwa, *Member, IEEE*, Armando Marino, *Member, IEEE*, Andrea Berardi, C Isabella Bovolo, Peter Hunter, Claire Neil, and Thiago S. F. Silva

***Abstract*—Quantifying flood inundation beneath vegetation is critical for understanding flood dynamics in complex wetland environments, where conventional remote sensing approaches often struggle to distinguish between open-water flooding and vegetation-covered inundation. In this study, we propose four novel detectors for the characterization of both open flooding and flooding beneath vegetation using radar-based signal analysis. The methods are developed from two fundamental signal models: the additive model of optimization of power difference and the multiplicative model of optimization of power ratio. Our objective is to investigate additive signal changes can inform or be combined with multiplicative ones. Based on these models, we developed four detectors through different combinations: First, monomial unitary combination, which represents the product of additive and multiplicative models; Second, monomial combination, a parameterized product-based model; Third, linear combination, based on additive integration; Fourth, mixed combination, a data-driven approach. The proposed detectors demonstrated strong potential for quantifying two types of flooding open-water flooding and grassland flooding beneath vegetation with the data-driven detector achieving the best overall performance.**

***Index Terms*—Change detection, flood inundation mapping, flooding under vegetation, signal processing, synthetic aperture radar (SAR).**

I. Introduction

THIS article presents generalizations of polarimetric change-detection theory for quantifying the spatial and temporal dynamics of seasonal flooding in the Rupununi wetlands of Guyana. Flooding is both a natural ecological process and a hazard that can affect biodiversity, livelihoods, and human infrastructure [1], [2], [3]. In wetlands, however, seasonal inundation also supports ecosystem processes, influences species distribution, and contributes to soil-carbon storage [4], [5], [6]. Accurately distinguishing open and vegetated flooding is important for understanding the spatial and temporal extent of inundation and distinguishing natural hydrological variability from changes associated with anthropogenic activities, such as infrastructure development and agriculture. This provides stakeholders with more actionable information on how flooding propagates across heterogeneous, seasonally flooded wetlands and which areas are repeatedly affected.

Optical remote sensing has been used to monitor flooding in wetlands using Landsat, Sentinel-2, and MODIS [7], [8]. The mapping achieved high accuracy in open water and areas that have sparse vegetation by utilizing bands, such as short wave infrared and near infra-red and thresholding methods to separate water from nonwater features [9]. Supervised and unsupervised classification methods have been applied on different datasets. Besides spectral bands, spectral water indices, including normalized difference water index (NDWI), modified NDWI, automated water extraction index, and normalized difference vegetation index, have been widely employed in combination with thresholding generated from data driven optimization techniques or histogram analysis [7], [10]. Other techniques, such as those utilizing machine learning approaches, specifically Random Forests, integrate multisource data, including optical imagery, radar data, and topographical indices, have been utilized with high accuracy [11], [12]. Although these methods are transferable, the reliance on optical data, have limitations, such as cloud coverage, operation on day time only and have low performance in areas with inundated vegetation [8], [13].

Synthetic aperture radar (SAR), which is unaffected by cloud cover and sunlight, has become a reliable data source for flood mapping [14]. SAR data are widely used for operational flood mapping and emergency response, with flood extents extracted from Sentinel-1, ALOS PALSAR, RADARSAT-2, and TerraSAR-X/TanDEM-X across C-, L-, and X-bands and various polarizations [15], [16], [17], [18]. Sentinel-1 operates in the C-band at a wavelength of approximately 5.6 cm. At this wavelength, backscatter is sensitive to vegetation characteristics and water-depth variations, with the observed response depending on vegetation density and morphology [19].

Received 1 May 2026; revised 18 August 2026; accepted 26 September 2026. Date of publication 1 October 2026; date of current version 26 October 2026. This work was supported in part by the Natural Environment Research Council via an IAPETUS2 Ph.D. studentship held by Isundwa Kasiti Felix under Grant NE/S007431/1 and in part by the Scottish Environment Protection Agency. *(Corresponding author: Felix Kasiti Isundwa.)*

Felix Kasiti Isundwa, Armando Marino, Peter Hunter, and Thiago S. F. Silva are with the Faculty of Natural Sciences, University of Stirling, FK9 4LA Stirling, U.K. (e-mail: f.k.isundwa@stir.ac.uk).

Andrea Berardi is with the Faculty of Science, Technology, Engineering and Mathematics, The Open University, MK7 6AA Milton Keynes, U.K..

C Isabella Bovolo is with the Department of Geography, Durham University, The Palatine Centre, DH1 3LE Durham, U.K..

Claire Neil is with Scottish Environment Protection Agency, Strathallan House, FK9 4TZ Stirling, U.K..

Digital Object Identifier 10.1109/JSTARS.2026.3739494

© 2026 The Authors. This work is licensed under a Creative Commons Attribution 4.0 License. For more information, see https://creativecommons.org/licenses/by/4.0/

Although open-water inundation commonly reduces backscatter, inundation beneath vegetation can increase backscatter and produce phase changes associated with double-bounce scattering [20]. Consequently, C-band backscatter may decrease, increase, or change only slightly across a flooded wetland, depending on vegetation structure and scattering conditions [19]. Change detection, thresholding, and object-based image analysis have been applied to flood mapping [21], while hierarchical classification of L-band SAR data has enabled accurate monitoring of open-water and microphyte flooding [22]. Recent studies have also applied supervised deep-learning models to Sentinel-1 flood-water extraction, using multisource inputs, such as water indices and terrain features, to improve segmentation and temporal monitoring [23], [24], [25]. Although these data-driven methods can achieve accurate scene-specific extraction, they generally depend on labeled training data and do not explicitly model the physical changes in polarimetric scattering associated with inundated vegetation. These limitations make a single intensity threshold or a model based solely on backscatter reduction unsuitable for reliably mapping both open water and inundated grassland.

Although polarimetric decomposition has been applied to flooded vegetation, including approaches combining Sentinel-1 C-band and ALOS-2/PALSAR-2 L-band data [26], comparatively less attention has been given to using Sentinel-1 C-band polarimetric change detection to characterize the scattering changes between nonflooded and flooded vegetation. The relevant problem is therefore to characterize the change in the polarimetric scattering state between nonflooded and flooded conditions. This motivates the use of Sentinel-1 single look complex (SLC) polarimetric data and analytically optimized change detectors that can account for transitions between volume-dominated and double-bounce scattering. Accordingly, previously proposed models [27], [28] are generalized and compared to assess their representation of backscatter variation and improve the detection of vegetated flooding.

This article introduces several novelties to flood mapping as follows.

1) We are proposing a generalization of polarimetric change-detection theory, by deriving three new analytical optimization that combine sets of previous detectors.
2) We are proposing a new detector that can quantify open and grassland flooding and improves separability of flood and no-flood areas.
3) We have applied Sentinel-1 SLC polarimetric change detection in mapping open and flooding under short vegetation (grassland) in a wetland environment improving the understanding of flood dynamics.

II. Methodology

A. Study Area

The Rupununi River catchment, a tributary of the Essequibo River, is located in the southwestern part of Guyana. Annually, this region experiences seasonal rainfall that floods vast areas of savanna. This flooding creates a seasonal connection between the Essequibo and Amazon Rivers, leading to ichthyofaunal exchange through a connection commonly referred to as the "Rupununi Portal" [29]. This phenomenon is ecologically significant for fish migration and reproduction. The hydrological connection between the different drainages is because of flooding of the low-lying Rupununi savannas which has been previously established to have extended over 3480 Km^2 on average (1967–1996) annually and the flood duration is highly variable in a year [30]. The floodplain is characterized by a treeless grassland as well as Mauritia palm swamps [31], [32]. Therefore, it is important to understand the flooding patterns within the region. For this reason, in this study, we are investigating the seasonal trends of floods during the rainy season between May and September from 2016 to 2023 to identify where and when floods occur in the region. For this analysis, we have selected a section of the Rupununi catchment for analysis as shown in Fig. 1.

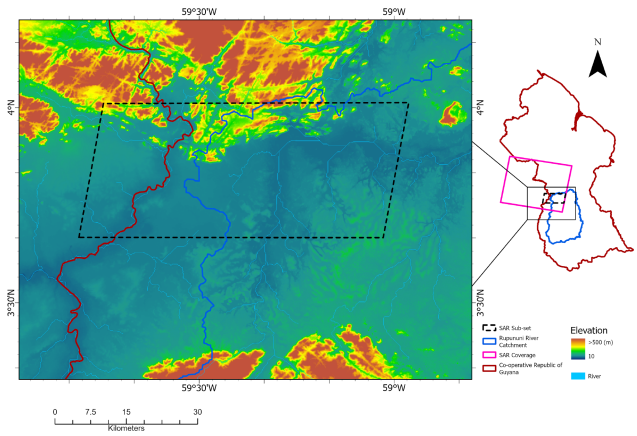


Fig. 1. Map of the study areas selected with reference to the Satellite data footprint. The dashed line represent the area selected for analysis in this study from the full SAR scene.

B. Data

The analysis in this study involved the preprocessing, and coregistration of Sentinel-1 C historical interferometric wide (IW) SLC data. A total of 214 images that were analyzed were acquired from 2016 to 2023. The data acquired in descending orbit at track 83 from the IW swath mode. Detailed documentation on the preprocessing and coregistration steps is documented in here [33]. The outputs of the preprocessing prior to coregistration produces the dual-pol covariance matrix elements C_{11}, C_{22}, and C_{12} which are the intensities of VV and VH, and the cross correlation between the VV and VH.

C. Preparation of Accuracy Assessment Data

PlanetScope optical data acquired on 03 July 2017 were used to assess the accuracy of assessment. The images are georeferenced orthomosaics generated through photogrammetric processing, involving the automated stitching and radiometric balancing of over 1000 overlapping aerial photographs per site acquired via a preprogrammed, grid-based UAV survey [34], [35], [36], [37], [38], [39], [40], [41], [42]. Drone data acquired 20 February 2020 with a 5-cm resolution were used to validate

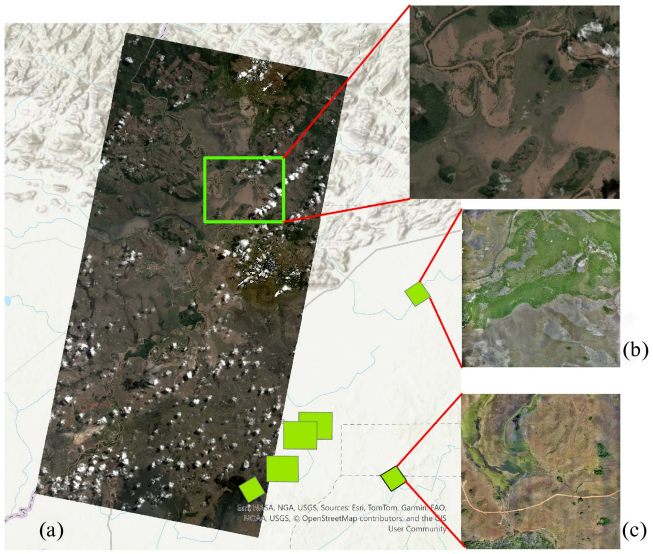


Fig. 2. Optical image used for accuracy assessment. (a) PlanetScope image acquired on 03 July 2017 (cm resolution). (b) and (c) Sample drone images acquired in 12 February 2020 with 5 cm resolution.

TABLE I
TABLE SHOWING SAR DATA ACQUIRED BY SENTINEL-1 DATA AND THE PLANETSCOPE OPTICAL IMAGE USED IN THE ACCURACY ASSESSMENT AND THE AREAS OF FLOOD AND NO FLOOD AREAS DIGITIZED FROM OPTICAL AND DRONE DATA

Sentinel-1 date (time)	PlanetScope date (time)	Grassland flood	Grassland no-flood	Open flood	Open no-flood
03 July 2017 (09:45)	03 July 2017 (13:35)	316.6	650.1	970.5	4548.9

The units of the areas are in hectares.

the classes identified from PlanetScope images as shown in Fig. 2. Flood and no-flood data were digitized from optical images into polygons shapefiles in a GIS environment. The optical data were acquired on the same day as the SAR data as show in Table I. The digitized datasets are then categorized into four classes. Open flood area and grassland flood areas, no-flood open areas and nonflood grasslands. The digitized shapefiles were then rasterized into the same resolution and extent as the SAR images for consistent analysis. Over estimation or underestimation may occur due to the slight time difference between the SAR and optical image acquisition. When carrying out accuracy assessment, we tested grassland flooding, open flooding, and the combination of both grassland and open floods.

D. Model

The eigenvalue decomposition of the polarimetric coherency matrix provides a physically meaningful characterization of scattering diversity across land cover types, yet the interpretation of the resulting parameters is critically sensitive to the number of polarimetric channels available and to the distributional structure of those eigenvalues [43], [44], [45]. In the present study, dual-polarimetric Sentinel-1 data in VV and VH polarizations are employed, yielding a 2×2 covariance matrix) and consequently only two real nonnegative eigenvalues $\lambda_1 \geq \lambda_2 \geq 0$ [46]. The polarimetric entropy H, derived from the two pseudoprobabilities, quantifies the degree of scattering randomness within the resolution cell: a strongly dominant λ_1 with negligible λ_2 indicates a low-entropy, near-deterministic scattering process, whereas approximately equal eigenvalues indicate a depolarizing mixture of mechanisms and $H \to 1$ [44]. It should be noted that the classical anisotropy parameter A, which requires a third eigenvalue from full polarimetric data, is unavailable in this dual-pol configuration, reducing the decomposition space to the $H/\bar{\alpha}$ plane alone and limiting the discrimination of secondary scattering mechanisms [46], [47].

In the context of wetland and savanna grassland environments, the question of whether fully developed randomness is achieved is particularly consequential for dual-pol systems. Short grassland vegetation ($\sim$1 m) presents a structurally intermediate scattering regime: randomly oriented grass elements generate a measurable cross-polarized return sufficient to elevate λ_2, yet a persistent coherent contribution from the underlying surface prevents the coherency matrix from approaching the isotropic limit [45], [46], yielding moderate entropy and leaving the dominant mechanism ambiguous in the compressed two-eigenvalue space. This eigenvalue structure determines which scattering mechanisms can realistically be identified when flood inundation occurs, and two physically distinct scenarios must be considered. In the first, rising water overtops or displaces the vegetation, producing open inundation/open floods and a transition to specular reflection; this is characterized by a sharp reduction in entropy, a strongly dominant λ_1, and a marked decrease in cross-polarized backscatter [48], [49]. In the second scenario, flooding occurs beneath standing grass without overtopping, allowing the SAR signal to penetrate the canopy and interact with the vertical stem-water interface; under these conditions, double-bounce scattering is expected to develop, elevating the copolarized VV return and increasing the overall backscatter relative to the preflood bare surface [48], [49]. However, it must be acknowledged that the absence of HH polarization in the Sentinel-1 VV+VH configuration limits the unambiguous discrimination of double-bounce from volume scattering, since the HH/VV ratio is the classical diagnostic of dihedral interactions and is not directly accessible here. When performing change detection between a preflood acquisition dominated by rough surface scattering and a coflood or postflood acquisition, both scattering mechanism transitions may be present simultaneously within the same scene, each manifesting differently in the dual-pol eigenvalue structure. It is with this physical complexity, and with the inherent constraints of the dual-pol observation space, that the present study aims to develop a flood detector capable of identifying and discriminating both open-water and vegetated-flood inundation across grassland and wetland environments. Different scattering mechanisms from flood environments are as shown in Fig. 3.

E. General Model for Change Detection

We aim to generalize the signal models introduced in [27] and [28] to provide a more flexible and robust way to detect

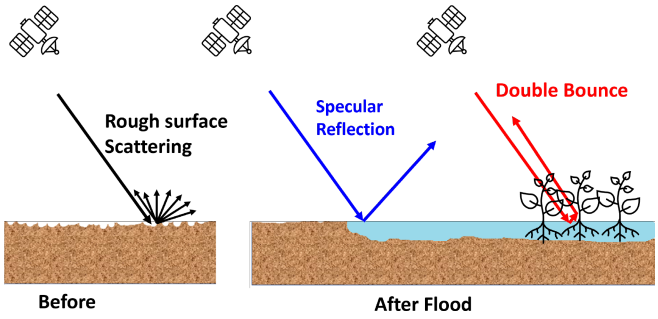


Fig. 3. Figure depicting the the three scattering mechanisms that occur in an environment with short vegetation and bare ground before and after the floods.

changes in SM. In this article such algorithm is applied, particularly to distinguish open water and flooded vegetation from nonflooded areas. To begin, we consider the two basic models, the additive model with the optimization of power difference (OPDiff) and the multiplicative model of optimization of power ratio (OPRatio) [27], [28]. Step by step derivation of the OPRatio and OPDiff have been elaborately described in [27] and [28] and will be omitted in this work. We start by defining two quadratic forms of the covariance matrix based on the difference and ratio as shown in (1) and (2), respectively. These simpler additive and multiplicative models are our building blocks for more complex processes, where we want to depict relations between these two simpler models. That is to say we want to model how an additive change could "bring/facilitate" a multiplicative one

$$\rho_d = \underline{\omega}^H (\mathbf{C}_2 - \mathbf{C}_1)\underline{\omega} \tag{1}$$

$$\rho_r = \frac{\underline{\omega}^H \mathbf{C}_2 \underline{\omega}}{\underline{\omega}^H \mathbf{C}_1 \underline{\omega}} \tag{2}$$

where $\mathbf{C}_1$ and $\mathbf{C}_2$ are covariance from two different acquisition times or condition, $\underline{\omega}$ is the complex projection vector, and ^{H} denotes the Hermitian (conjugate) transpose, and ρ_d and ρ_r are defined as quadratic forms of covariance matrices $\mathbf{C}_1$ and $\mathbf{C}_2$, respectively. Specifically, in this study, $\mathbf{C}_1$ represents the covariance matrix of the image acquired before a flood while $\mathbf{C}_2$ is the one acquired during/containing flooded areas.

1) Model 1—Monomial unitary combination: In the first attempt to generalize the signal models to be able to represent more complex dynamics, we use the monomial unitary combination. This is able to depict links between the simpler models due to correlations. That is a addition that also bring a transformation. We combine the two quadratic forms via multiplication, shown as follows:

$$M_1 = \rho_d \cdot \rho_r. \tag{3}$$

Substituting (1) and (2) into (3) yields

$$M_1 = \underline{\omega}^H (\mathbf{C}_2 - \mathbf{C}_1)\underline{\omega} \cdot \frac{\underline{\omega}^H \mathbf{C}_2 \underline{\omega}}{\underline{\omega}^H \mathbf{C}_1 \underline{\omega}}. \tag{4}$$

Simplify optimization by applying whitening using $\mathbf{C}_2$. Define the transformed matrix and vector

$$\mathbf{C}_m = \mathbf{C}_2^{-1/2} \mathbf{C}_1 \mathbf{C}_2^{-1/2}. \tag{5}$$

This transformation assumes $\mathbf{C}_2$ is full rank. Substituting into M_1

$$M_1 = \underline{\omega}^H (I - \mathbf{C}_m)\underline{\omega} \cdot \frac{\underline{\omega}^H I \underline{\omega}}{\underline{\omega}^H \mathbf{C}_m \underline{\omega}} = \frac{\underline{\omega}^H (I - \mathbf{C}_m)\underline{\omega}}{\underline{\omega}^H \mathbf{C}_m \underline{\omega}} \tag{6}$$

where I is the identity matrix.

To maximize or minimize M_1, we optimize the numerator subject to a constraint on the denominator. Specifically

$$\underline{\omega}^H (I - \mathbf{C}_m)\underline{\omega} \tag{7}$$

subject to

$$\underline{\omega}^H \mathbf{C}_m \underline{\omega} = 1. \tag{8}$$

This is a standard Rayleigh quotient optimization. We use the Lagrangian

$$\mathcal{L} = \underline{\omega}^H (I - \mathbf{C}_m)\underline{\omega} + \lambda \left(1 - \underline{\omega}^H \mathbf{C}_m \underline{\omega}\right). \tag{9}$$

Taking the derivative with respect to $\underline{\omega}^H$ (for complex vectors) and setting to zero

$$\frac{\partial \mathcal{L}}{\partial \underline{\omega}^H} = \frac{\partial}{\partial \underline{\omega}^H} \left[(I - \mathbf{C}_m)\underline{\omega} - \lambda \mathbf{C}_m \underline{\omega}\right] = 0. \tag{10}$$

Rearranging

$$(I - \mathbf{C}_m)\underline{\omega} = \lambda \mathbf{C}_m \underline{\omega} \tag{11}$$

$$\mathbf{C}_m^{-1}(I - \mathbf{C}_m)\underline{\omega} = \lambda \underline{\omega}. \tag{12}$$

This is a generalized eigenvalue problem. The extrema of M_1 are the eigenvalues λ, and the optimal $\underline{\omega}$ are the corresponding eigenvectors. This completes the first model for combining the optimizations. From this model, we get the maximum and minimum eigenvalues and refer them to as Mon$U1$ and Mon$U2$.

2) Model 2—Monomial combination: In the second model, we want to represent changes where an addition provides a transformation (or vice versa), but the effect of each block is not equal. For instance we need an exponentially larger addition to introduce a transformation. Therefore, we are combining ρ_d and ρ_r by multiplication with parameters β and γ shown as follows:

$$M_2 = \rho_d^{\beta} \cdot \rho_r^{\gamma}. \tag{13}$$

Substituting (1) and (2) into (13) produces

$$M_2 = \underline{\omega}^H (\mathbf{C}_2 - \mathbf{C}_1)\underline{\omega}^{\beta} \cdot \left(\frac{\underline{\omega}^H \mathbf{C}_2 \underline{\omega}}{\underline{\omega}^H \mathbf{C}_1 \underline{\omega}}\right)^{\gamma}. \tag{14}$$

We simplify the equation by applying a whitening using $\mathbf{C}_2$ with similar definitions from (5) as follows:

$$M_2 = \underline{\omega}^H (I - \mathbf{C}_m)^{\beta} \underline{\omega} \cdot \frac{\underline{\omega}^H I \underline{\omega}}{\underline{\omega}^H \mathbf{C}_m^{\gamma} \underline{\omega}}. \tag{15}$$

Simplifying the (15), performing a Lagrange optimization and taking the partial derivative with respect to $\underline{\omega}^H$ and equating it 0 as follows:

$$\frac{\partial \mathcal{L}}{\partial \underline{\omega}^H} = \frac{\partial}{\partial \underline{\omega}^H} \left[\underline{\omega}^H (I - \mathbf{C}_m)^{\beta} \underline{\omega} - \lambda \underline{\omega}^H {\mathbf{C}_m}^{\gamma} \underline{\omega}\right] = 0 \tag{16}$$

$$(I - \mathbf{C}_m)^{\beta} \underline{\omega} = \lambda {\mathbf{C}_m}^{\gamma} \underline{\omega}. \tag{17}$$

Rearranging (17) as follows:

$$\mathbf{C}_m^{-\gamma}\left(I-\mathbf{C}_m\right)^{\beta}\underline{\omega}=\lambda\underline{\omega}. \tag{18}$$

We tested multiple parameters of β and γ to determine the one that best model the change and therefore provides the highest accuracy. The values ranged from 0 to 5. These parameters were set by fixing one and varying the other such that if we fix $\beta=1$, then γ values are tested ranging from 0 to 5 and vice versa. The final form of the equation is selected using the optimal parameter which give the highest receiver operating characteristic (ROC) curve (AUC).

This completes the second model of combining the optimizations. From this model, we get the maximum and minimum eigenvalues and refer to them as Mon1 and Mon2, respectively.

3) Model 3—Linear combination: Finally, we want to model a situation where an additive change can happen in parallel to a multiplicative one, but bot stay independent to each other. That is to say the addition does not bring a multiplicative transformation, but it merely happen at the same time. We are combining ρ_d and ρ_r by a summation while introducing a factor α which models change better providing the highest accuracy shown as follows:

$$M_3=\alpha\rho_d+(1-\alpha)\,\rho_r. \tag{19}$$

Substituting (1) and (2) into (19) gives

$$M_3=\alpha\underline{\omega}^H(\mathbf{C}_2-\mathbf{C}_1)\underline{\omega}+(1-\alpha)\left(\frac{\underline{\omega}^H\mathbf{C}_2\underline{\omega}}{\underline{\omega}^H\mathbf{C}_1\underline{\omega}}\right). \tag{20}$$

Simplify the equation by applying a whitening using $\mathbf{C}_1$

$$M_3=\frac{\alpha\underline{\omega}^H(\mathbf{C}_2-\mathbf{C}_1)\underline{\omega}\cdot\underline{\omega}^H\mathbf{C}_1\underline{\omega}+(1-\alpha)\,\underline{\omega}^H\mathbf{C}_2\underline{\omega}}{\underline{\omega}^H\mathbf{C}_1\underline{\omega}}. \tag{21}$$

If

$$C_r=\mathbf{C}_1^{-1/2}\mathbf{C}_2\mathbf{C}_1^{-1/2} \tag{22}$$

then

$$M_3=\alpha\underline{\omega}^H(\mathbf{C}_r-I)\underline{\omega}+(1-\alpha)\,\underline{\omega}^H\mathbf{C}_r\underline{\omega}. \tag{23}$$

Simplifying (23) as follows:

$$M_3=\alpha\underline{\omega}^H\mathbf{C}_r\underline{\omega}-\alpha\underline{\omega}^H\underline{\omega}+\underline{\omega}^H\mathbf{C}_r\underline{\omega}-\alpha\underline{\omega}^H\mathbf{C}_r\underline{\omega} \tag{24}$$

$\omega^H\omega=1$, then

$$M_3=\underline{\omega}^H\mathbf{C}_r\underline{\omega}-\alpha. \tag{25}$$

Optimizing using Lagrange leads to

$$\mathbf{C}_1^{-1/2}\mathbf{C}_2\mathbf{C}_1^{-1/2}\underline{\omega}=\lambda\underline{\omega}. \tag{26}$$

After the derivation of the third model, we get the maximum and minimum eigenvalues and refer them to as Lin1 and Lin2.

4) Model 4—Mix combination: The final test is a detector that is more data driven using outputs from the OPDiff and OPRatio already described in [27] and [28]. From the additive model (OPDiff), we take the maximum eigenvalue of the change representing the maximum change of power of SM between two acquisition and refer to it as λ_d. From multiplicative model (OPRatio), we select the minimum eigenvalue from its corresponding eigenvector. We refer to the selected eigenvalue λ_r which represents the minimum ratio between two SM from two acquisitions. Subsequently, the next section considers and combines λ_d and λ_r to determine model 4. Equation (27) represents the combination of the variables by multiplication and the introduction of a combination factor

$$M_4={\lambda_r}^n\cdot{\lambda_d}^m \tag{27}$$

where n and m are combination parameters that maximize the difference between the flood and no floods. Ideally, we want a combination parameter that maintains negative values where the backscatter values dropped while positive and highest values when the backscatter increase. After determining the equation, we tested the values of n and m to obtain the optimal parameter for combination. The values resulting from this detector will be positive or negative where positive values will indicate areas of increase in backscatter while negative values will show areas of decrease in backscatter between two acquisitions. The output of model 4 is then abbreviated as $\text{Rat2}^n\cdot\text{Dif1}^m$ with the powers being the optimal n and m values selected.

Besides the four stated models, we are also comparing the performance against outputs from additive model OPDiff (Dif1 and Dif2) from maximum and minimum eigenvalues and from the OPRatio where Rat1 and Rat2 are maximum and minimum eigenvalues. We also tested and compared the detection with methods, such as the ratio of backscatter intensity in the VV and VH, and referred to as RatVV and RatVH.

F. Physical Interpretation of Detectors

For more information on the physical the interpretation of OPDiff and OPRatio see [27] and [28] where OPDiff is adding/removing the scattering mechanisms and where OPRatio is transforming it. The proposed detectors do not only have a mathematical but also a physical interpretation.

1) *Monomial unitary combination detector:* This detector considers situations where the additional/removal of scattering mechanisms between two acquisitions also bring about transformation and the two are equally weighted. That is, the change models are not decoupled, and that additive and transformative changes occur simultaneously and are correlated. For example, when in a grassland environment, grass growth and tilt brings about addition of scattering and transformation of the scattering. In a flood under grassland scenario, the increase in backscatter from double bounce scattering from vegetation–water interactions will bring both the additional in scattering power and transformation of rotated/tilted grass.
2) *Monomial combinations:* This detector considers that the addition/removal of scattering mechanisms between two acquisitions bring about transformation, however, the two components impact the transformation differently (not equally). That is to say, the additional of scattering mechanisms and the rotation/transformation of the targets are not equal in weight. In a grassland environment, the growth of grass and the rotation of grass would be manifested with different weights (which are at the exponent).

3) *Linear combinations:* This detector considers that the addition/removal and/or transformations of scattering mechanisms between two acquisitions occur independently. That is to say, the changes are decoupled and are independent of each other. In the case of vegetation, there could be that some of the pixels in the averaging cell get fully flooded and the vegetation scattering disappear (removal of scattering mechanism), and the other pixels suffer a tilting of the vegetation (rotation of the scattering mechanism). That is the tilting and the growth happen in different pixels and independently inside the same averaging cell.
4) *Mix combinations:* This detector continues in the line of the monomial reasoning, where the components of change are dependent/correlated but it tries to decouple the phenomena by optimizing the two problems separately. It considers that the minimum power of transformation of the target between the two acquisition occurs at the same time as the maximum power of scattering mechanism addition/removal. Indeed, this mixing makes the physical interpretation harder and moves more toward a mathematical model but in its core it considers correlated change phenomena but try to decouple their optimization to find the best optima for each of the phenomena separately (which brings different optima then when trying to do this in a single optimization).

G. Accuracy Assessment

For each pixel, the reference covariance matrix used for change detection was calculated as the mean of all images acquired in March across all years on record. This approach was informed by earlier findings [18], which showed that using the mean of March images across the years on record provided better performance for time-series analysis. March is characterized by cleared land in preparation for the rainy and planting seasons, with minimal crop cover.

The accuracy of the detectors was assessed using the data prepared in Section II-C. The best temporal match between the SAR and optical data was obtained using the SAR image acquired on 03 July 2017 and the corresponding optical image acquired on the same day. Detector performance was assessed using a semisupervised approach based on the area under AUC. AUC was selected as a threshold-independent measure of detector performance.

In addition to AUC, threshold-dependent metrics were calculated, including accuracy, probability of detection (PD), probability of false alarm (PF), and F1-score. In the semisupervised approach, accuracy assessment data were digitized from the optical imagery and used as reference data. An array of threshold values spanning the minimum to maximum values of each change-detection result was evaluated. For each threshold, the PD, PF, accuracy, and F1-score were calculated. The threshold providing the best overall performance was then selected and the corresponding metrics recorded. The threshold should have a PD of at least 0.85, an accuracy of at least 0.85, and a PF of no more than 0.20. These threshold-dependent metrics were estimated using the semisupervised methodology described by Isundwa et al. [18].

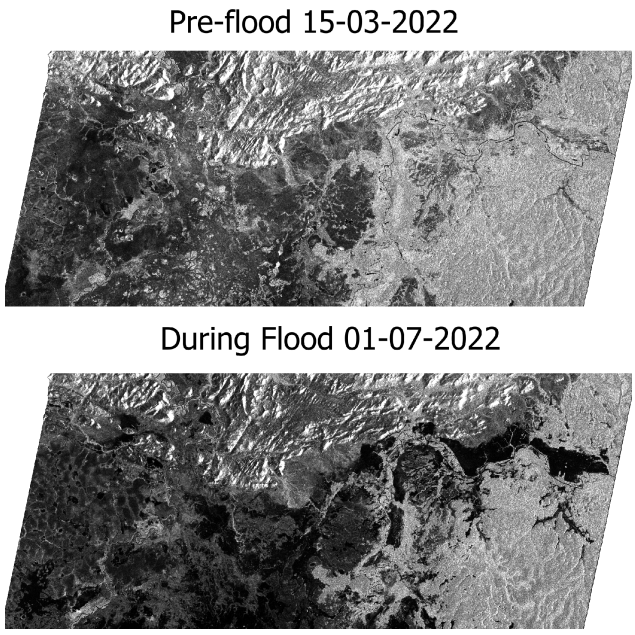


Fig. 4. Figure showing the preflood and postflood images on record of backscatter intensity of VH channel.

III. Results

A. Visualization of SAR Data (Dry and Flood Image)

We first inspect sample images acquired before and during a flooding. From Fig. 4, we show one acquisition on 15 February 2022 during a dry season and just before the onset of the rainy season and an acquisition from 01 July 2022 during the rain season. These acquisitions show the backscatter intensity in VH polarization. The plots show different backscatter characteristics displayed. There are areas where there is decrease in backscatter occasioned by open floods. There are also areas where there is increased backscatter but are not clearly distinct in the flood image. The vegetated areas are bright due to stronger backscatter in the VH.

B. Model Tuning

Two detectors proposed are flexible and can be tuned. We carried the tuning of the first flexible model (Model 2) by tuning factors β and γ to determine the optimal factor. These factors should give the best AUC when classifying flood and nonflood areas. From the analysis, and after testing the multiple factors, there were observable difference in performance only when either factor is set to 0. Therefore, we selected the factors $\beta = 2$ and $\gamma = 1$ since they had highest accuracy of open-flood and no-flood separability. Another Model that needed tuning was model 4 where the factors m and n were tested and determined after change detection. These are factors that maximize the separation distance between flood and nonflood values for open and grassland floods. We tested multiple factors as shown in Fig. 5. From this analysis, we established that $m = 2$ and $n = 1$ are the

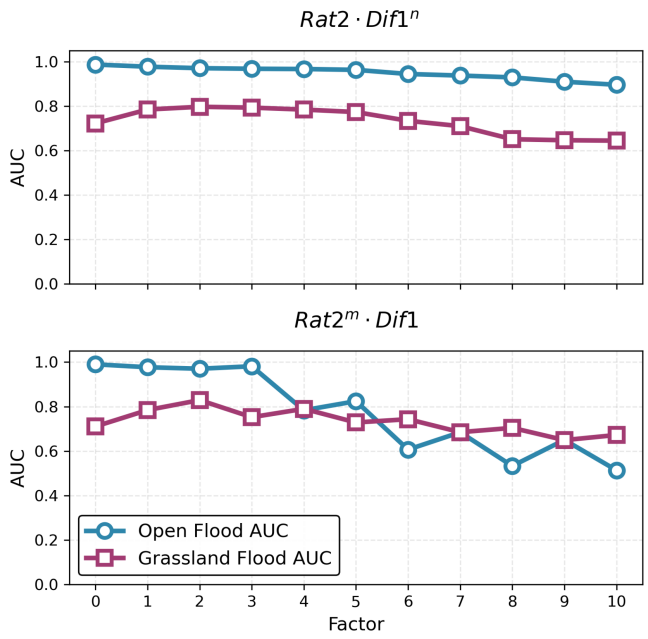


Fig. 5. Plot of combination parameter m and n tested. The top subplot was tested by fixing $m = 1$ and varying n, while the bottom plot was tested by fixing $n = 1$ and varying the m variable.

optimum factors that gives the highest AUC in distinguishing grassland and open floods from nonflooded areas. Therefore, from (27), we get $M_4 = {\lambda_r}^2 \cdot \lambda_d = \text{Rat2}^2 \cdot \text{Dif1}$. That is the square of the minimum eigenvalue from the OPRatio multiplied by the maximum eigenvalue from OPDiff.

Fig. 6 visually represents the combination and the resulting output spatially. We can observe that from Dif1, there are open flood areas observed as blue containing negative values while other areas which have grassland and other cover types as red and positive values. White areas are those that did not undergo any or very minimal change. The second input Rat2 shows value of no change close to 0 while higher changes tend to be greater than zero. These areas include both open and grassland flooded areas. A closer look at the output of combination shows an interesting phenomenon. Open flood areas are blue areas with negative values while areas where there is grassland flooding are red and with positive values. There is also clear distinction between flood and nonflood areas which appear white with values close to zero.

C. Flood and No-Flood Separability

The third step after performing the optimization was to understand how each optimization separate flooded from nonflooded areas. We are looking at the separability in the search space where the detector performs the optimization. This was checked with a scatter plot of pixels of regions digitized from optical data. The scatter plot shows four classes of which two are flood areas (open and grassland floods) and the remaining are nonflood areas (open no-flood and grassland no-flood areas) as shown in Fig. 7. The plot shows varying separability from detectors. To begin, the backscatter intensity data VV is plotted against VH showing overlap between flood and no-flood classes. After the

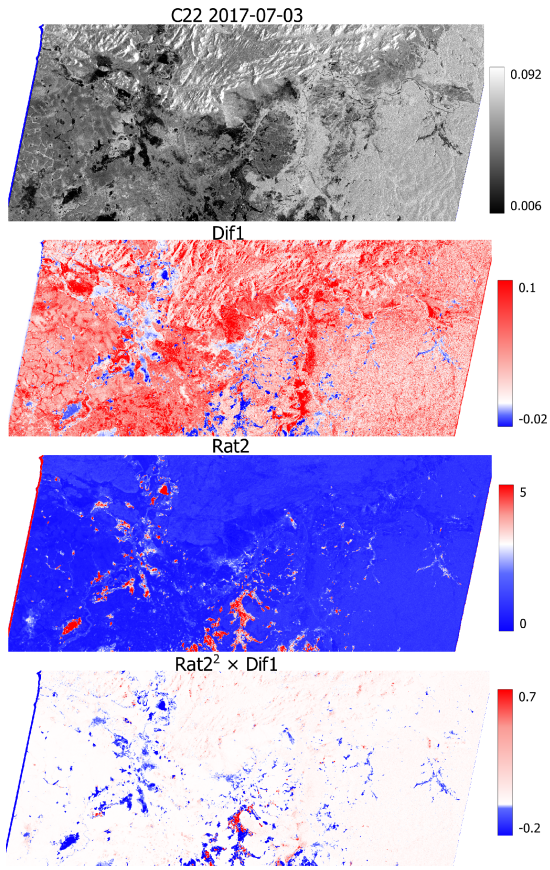


Fig. 6. Figure of the spatial representation of combination of Rat1 and Dif1 with reference to the VH image backscatter intensity image.

optimizations, Rat1 plot against Rat2 shows better separability between open flood and nonflooded areas. For Rat1, there is a mix between grassland floods and no-flood areas. Rat2 shows similar characteristic, however, the open and grassland flood overlap but are better separated from no-flood areas. Dif1 shows better separability of open floods only. Dif2 on the other hand visually shows better separability of floods and no-floods in general. Lin1 and Lin2 are better at separating flood from open flood areas. RatVH is better at separating flood and nonflooded areas while RatVV can only separate open floods from other classes. Mon$U1$ is better at flood and no-flood separation but and has high overlap between open and grassland flood, Mon$U2$ showing open flood separation only. Mon1 shows better combined flood separability from nonflood classes while Mon2 shows open flood separability. These two also have grassland flood separability but with high degree of overlap. $\text{Rat2}^2 \cdot \text{Dif1}$ combines the search spaces of Rat and Dif in a peculiar way. It is therefore no point to show it as a scatter plot and we used box-plots. It shows very distinct feature compared to all others. Open flooded are distinct from grasslands floods with the two also being distinct from no-flood areas. The no-flood classes areas spread around zero, open flood values being less than zero while grassland values spread to above zero. In summary, from the analysis of the detector separability, $\text{Rat2}^2 \cdot \text{Dif1}$ is the only detector that isolates open floods, grassland floods and no-flood areas better. Rat1, Dif1, Lin2, Mon$U2$, Mon2, and RatVV show better open-flood

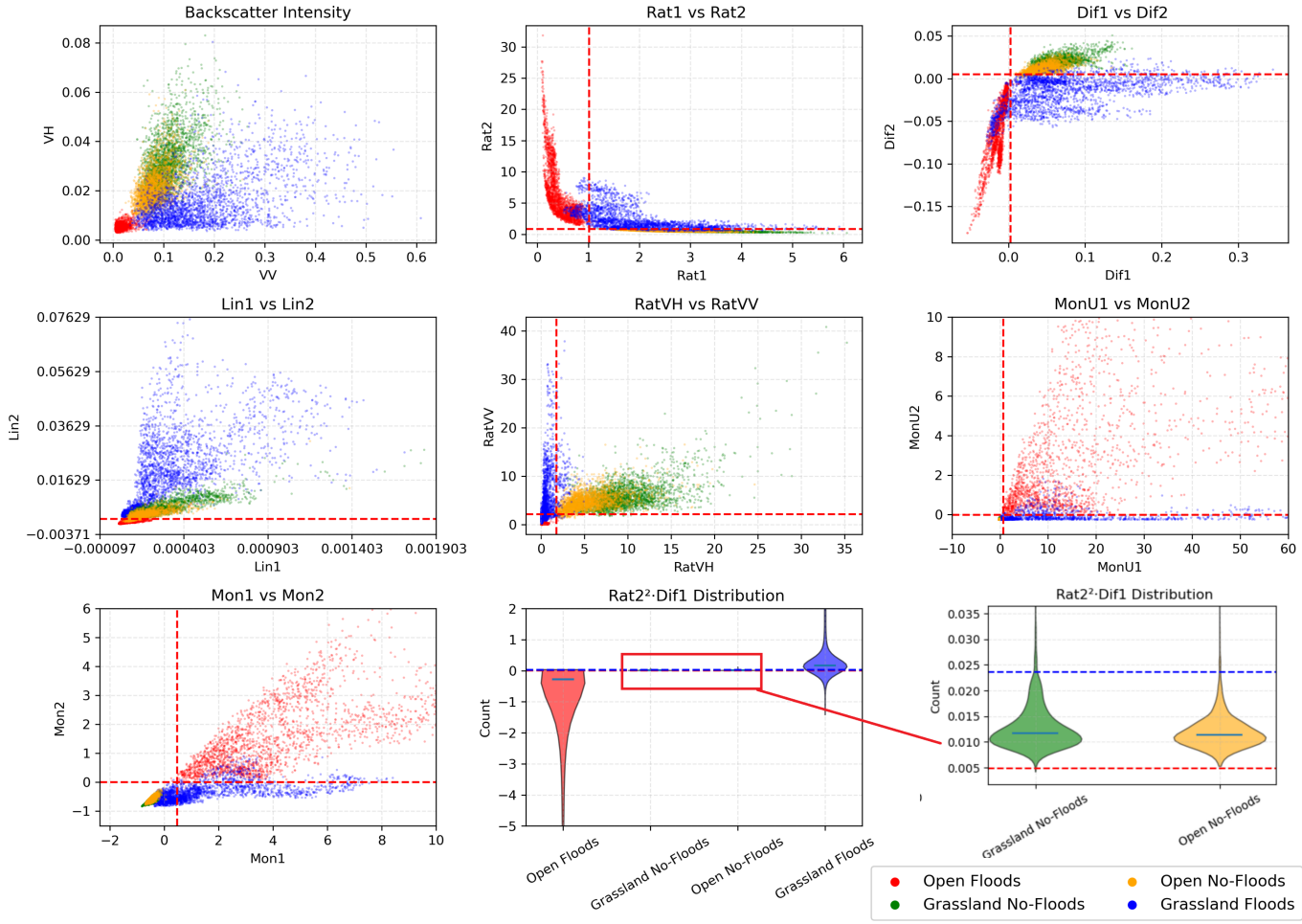


Fig. 7. Scatter plots of flood and no-flood areas. The scatter plots are plots of each detector plotted against VH polarization of the flood image (03 July 2017). Open floods are represented by red dots, grassland floods with blue dots, open areas which are not flooded by orange, and grassland areas not flooded by green. The red dashed line represent the thresholds of separating open floods from nonflood areas while the blue dashed line represent threshold for separating grassland flood from open and nonflooded areas.

separability from other classes. Mon1, Mon$U1$, Rat2, Dif2, and RatVH, show general separability of flood (open and grassland) from no-flood areas.

D. Quantitative Performance of Detectors

The fourth analysis step, after deriving the detectors and evaluating their separability, was to quantify their performance using flood and nonflood reference areas digitized from optical imagery. We sought to understand if and how accurately the detectors distinguish between open and grassland floods or both. The assessment used threshold-dependent metrics, including accuracy, PF, and PD, together with the threshold-independent AUC. As discussed in Section II-C, we selected one image for accuracy assessment. The open-water results are not discussed separately because most detectors achieved high performance for this class. The results of the accuracy assessment are shown in Table II.

Only four detectors distinguished grassland flooding from open-water flooding: Mon1, Rat$2^2 \cdot$ Dif1, Mon$U1$, and Mon2. Rat$2^2 \cdot$ Dif1 has the highest AUC and accuracy for detecting grassland floods, while the other three have poor performance.

TABLE II
MEAN VALUES OF PERFORMANCE METRICS FOR THE DIFFERENT METHODS FROM ALL DATES ANALYZED

Detector	AUC		Accuracy		PF	
	Grass.	Both	Grass.	Both	Grass.	Both
$Dif1$	-	0.854	-	0.894	-	0.01
$Dif2$	-	0.986	-	0.983	-	0.01
$Rat1$	-	0.923	-	0.924	-	0.02
$Rat2$	-	0.997	-	0.984	-	0.01
$Rat2^2 \cdot Dif1$	0.820	-	0.918	-	0.02	-
$Mon1$	0.711	0.996	0.715	0.984	0.25	0.01
$Mon2$	0.731	0.935	0.719	0.924	0.20	0.02
$MonU1$	0.663	0.991	0.715	0.984	0.25	0.01
$MonU2$	-	0.960	-	0.933	-	0.02
$RatVH$	-	0.979	-	0.987	-	0.01
$RatVV$	-	0.910	-	0.911	-	0.03

The highlighted cell colours indicate the best metric (green) and worst metric (red). Columns represent the AUC, accuracy and PF for each detector for grassland and both (open and grassland) flood.

Rat$2^2 \cdot$ Dif1 also produced the lowest PF, with a value of approximately 2%, whereas Mon1, Mon2, and Mon$U1$ produced PF values above 20%. Thus, Rat$2^2 \cdot$ Dif1 provided the clearest

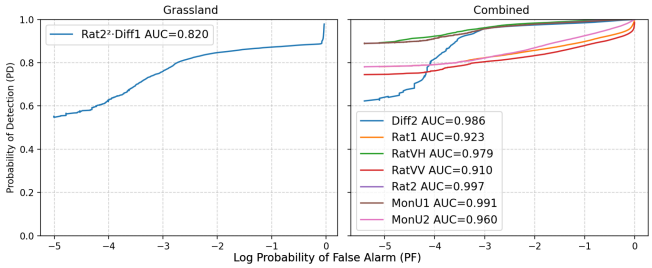


Fig. 8. ROC curve plot showing the PD against the the Log PF. The log is to help with the visualization of plots. The subplot on the left represents only ROC curves of detecting grassland floods while the one on the right represents the ROC curves of detecting a combination of grassland and open floods or simply flooded areas.

separation between open-water and grassland flooding while minimizing false alarms.

In detecting both open and grassland floods, most detectors have high AUC, accuracies, and lower PF rates. Rat2 had the highest AUC followed by Mon1 and Mon$U1$ with over 0.99 while Dif2, Mon$U2$, and RatVH had values above 0.96. Rat1 and RatVV had around 0.92. The detectors showed a similar trend in accuracy. The five best-performing detectors achieved approximately 98%, whereas the lowest accuracy was approximately 89%. All the detectors had low PF rates of less than 4%.

The different performance patterns are consistent with the distinct scattering responses represented by the detectors. Most methods effectively separated the combined flood class from nonflooded areas, but they were less successful at distinguishing open-water from grassland flooding. This distinction is more challenging because inundation beneath vegetation can modify the relative contributions of volume and double-bounce scattering rather than producing a unique reduction in backscatter. Overall, Rat$2^2 \cdot$ Dif1 was the only detector that reliably separated open-water floods, grassland floods, and nonflood areas. The remaining detectors were effective for general mapping of combined flooding, with high accuracy and low false-alarm rates, but did not provide the same level of separation between the two flood types.

E. ROC Plots of Classification

The ROC plot of the classification results show a similar characteristic as presented above and shown in Fig. 8. From the plot, when detecting grassland flooding, Rat$2^2 \cdot$ Dif1 maintains a steady and high PD values while having lower PF. This is similar to the observation from Table II. When detecting the combination of both grassland and open floods, Mon$U1$, RatVH, and Rat2 are the best at characterizing the general flooding scenario. Dif2 is the fourth best at general flood detection. Rat1, Mon$U2$ and RatVV are the least performing detectors with lower PD rates at low PF when detecting combined flooded areas.

In summary, Rat$2^2 \cdot$ Dif1 is the best detector tested for grassland flood detection with overall low PF. Rat2 is the best detector for detecting combined flooded areas (open and grassland). Mon$U1$ is the third best at detecting flooded areas with similar performance as Rat2 and RatVH. Interestingly, although these results are not shown, RatVV has approximately 3% better performance when considering the AUC in mapping open floods compared to RatVH. Similar margin is observed when looking at the highest accuracy. On the other hand, RatVH outperforms RatVV by approximately 6% in mapping combined open and grassland floods when considering the AUC. A similar margin is observed when looking at the accuracy of detection.

TABLE III
SUMMARY OF COMPUTATION TIME FOR THE DETECTORS AFTER PREPROCESSING

Model	Approximate Time (min)	
	NumPy Array Loop	Vectorized
OpRatio	18	0.19
OpDiff	18	0.19
RatVV/VH	–	0.11
Monomial Combination	37	0.22
Monomial Unitary Combination	37	0.22
Linear Combination	37	0.22
Mixed Combination	19	0.29

F. Flood Classification Comparison

This section compares classification results of selected detectors against a optical image and backscatter intensity VH from a flooded section overlaid by digitized areas with different flood types. Fig. 9 shows how the detectors isolated flooded from nonflood areas. From the figure, we can observe that there is variability in how flood and no-flood areas are separated. To begin, Rat1 is only able to pick out open flood areas while Rat2 detector is picks both open and grassland flooded areas as general flooded areas. These two detectors have minimal misclassification. Dif1 delineates only open flood areas. The Rat$2^2 \cdot$ Dif1 can quantify grassland and open flood areas with higher accuracy in open flood while grassland floods significant over detection. Lin1 and Lin2 detects open floods. RatVH is only able to quantify the combined flood areas with underestimation. Mon$U1$ is good at detecting both open and grassland floods with high accuracy. Mon1 detects combined floods while Mon2 underestimates the flooded areas.

G. Computation Efficiency

The methodologies applied in this research can be utilized in operational flood mapping exercise. The performance of the detectors was compared in terms of time take to process subset of the SAR scene. The subset is of approximate dimension of 39 Km $\times$ 88 Km. This was analyzed on Windows 11 Enterprise with AMD Ryzen 5 PRO 5650GE with Radeon Graphics (3.40 GHz) processors and 64.0 GB (63.3 GB usable) random access memory. The comparison of time taken between different methods are as shown in Table III. Two methods of analysis were tested: 1) a pixelwise loop using NumPy arrays, where change detection was performed for each pixel individually, and 2) a vectorized implementation, where change detection was applied to the entire array using NumPy's vectorized operations. The preprocessing time before change detection took approximately 10 min.

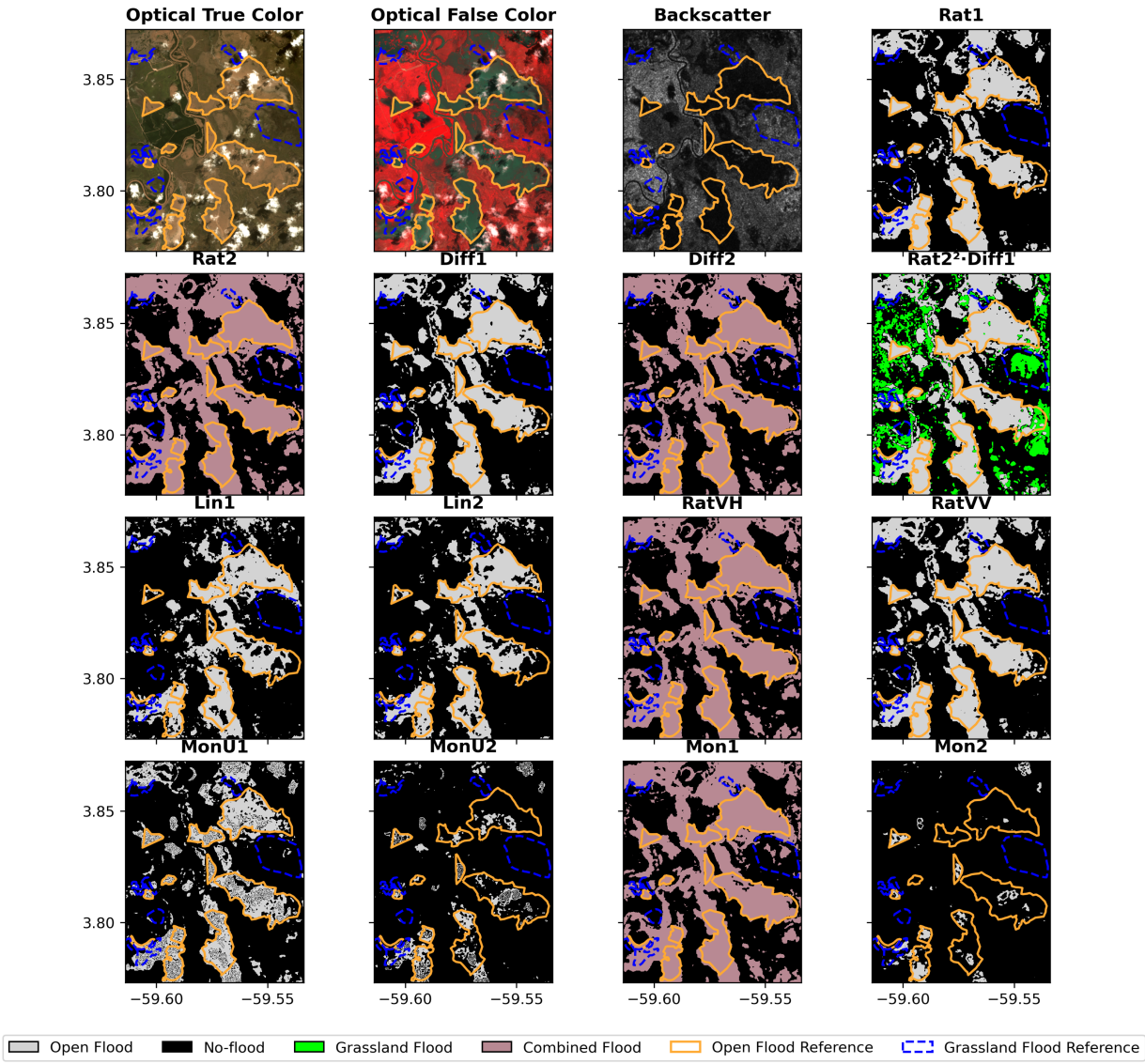


Fig. 9. Figure showing classification subplots for selected detectors. Black shows no-flood areas, orange is the combined open and grassland flooding, white is the open flood areas, and green representing flooded grassland areas. The first plot is the snippet from optical image from PlanetScope acquired on the same day as the SAR data with a approximately four hours difference. The plots are without any postprocessing.

IV. Discussion

In this study, signal models for polarimetric change detection were generalized by formulating additive and multiplicative combinations within an optimization framework. The objective is to assess whether increased modeling flexibility leads to improved flood discrimination performance. The application focuses on mapping inundated vegetated areas and distinguishing between open-water flooding and flooding under emergent vegetation in a wetland environment. Analytical expressions of physically interpretable change detectors are derived, and their performance is quantitatively evaluated using reference areas digitized from optical imagery. The proposed polarimetric detectors are further compared against conventional backscatter intensity-based change metrics.

The existing model of OPRatio and OPDiff demonstrated good performance in detecting flooded areas from nonflooded areas. This confirms earlier findings [18] where the performance was evaluated on open floods. The OPRatio detector was best at detecting open floods and the combination of grassland and open floods, while the difference was good at detecting open floods. From the OPRatio, Rat2 was best at detecting general flood from no-flood areas. Although the performance was good, these models could not separately quantify the areas of increase in backscatter due to grassland floods. The difference detector OPDiff had lower performance compared to the ratio-based detector. Although they both could quantify the open flood and no-flood areas, the difference is that in the latter, areas of removal of scattering power (open flood) had negative values while the areas of increase in scattering power (grassland flood) had positive values. Dif1 from the OPDiff gave the maximum power of the scattering mechanisms added or removed between two acquisitions.

The derived generalized signal models (monomial, monomial unitary, and linear forms) demonstrated the ability to separate flood from nonflood areas. The monomial combination model classified open and grassland flooding. However, this model was good at classifying a combination of both grassland and open flooding more accurately while it was poor at classifying grassland flooding. There was high overestimation of grassland flooded areas. A similar observation was made when considering the monomial unitary model. The third model, the linear combination was good at detecting open floods only while failing to quantify any areas of grassland flooding. From the analysis, although we developed these models to quantify changes better because they fit the data in better way, they do not perform better that the existing detectors of OPRatio. This may be attributed to the limited polarimetric information content in dual-pol data, which is already effectively exploited by OPRatio.

On the other hand, when a more data driven approach is applied, we get more information about the changes that occur between two acquisitions. Although the approach is data driven, it is still based on the physics. Here, Rat2 and Dif1 are combined into $\text{Rat2}^2 \cdot \text{Dif1}$ to form a new detector. This combination ensures that we maximize the power and maintain the negative values for open floods while areas with increase in double bounce are amplified and maintained positive values. Where no change occurs between acquisitions, values remain close to zero. The analysis established that the detector $\text{Rat2}^2 \cdot \text{Dif1}$ is the best detector that can quantify open floods and grassland vegetation separately and with high accuracy and low false alarms. The characteristic that makes open floods values negative and grassland flood value positive makes the detector able to have two distinct ways of getting the two flood types. This capability, unlike that of the other tested detectors, facilitates retrieval of more detailed information on distinct change mechanisms. This capability was applied to time series data showcasing the potential to retrieve seasonal and annual flood trends.

The backscatter intensity only analysis established that ratio of VV data ($\text{Rat}VV$) is good at open flood detection while VH ($\text{Rat}VH$) is good at detecting an area that experiences mixed open and grassland flooding. This finding is consistent with an earlier study [18].

In summary, although the generalized models provide improved physical consistency, they do not outperform the existing OPRatio detector. Interestingly, a more data driven detector $\text{Rat2}^2 \cdot \text{Dif1}$ enabled retrieval of more information about changes between two acquisitions quantifying open and grassland flooding while maintaining areas with no change. We have demonstrated that we can apply this detector in monitoring the dynamics of floods in a wetland. Future efforts will focus on testing and applying the polarimetric change detection in a densely forested-inundated areas and using longer wavelength data (L or P band).

V. Conclusion

This study derived and applied four new physically driven signal models of change detection to quantify flood dynamics in Rupununi region of Guyana. The article leveraged on the vast Sentinel-1 historical dual-polarimetric SAR data which are available freely to identify open and grassland flooded areas during the May–August rainy period from 2017 to 2023. The results were compared to the commonly used backscatter intensity flood detection methods using the VV and VH data. This was also compared with outputs from OPDiff and OPRatio. The mean of March images from all years on record was applied as the reference image. It was established that the new detector $\text{Rat2}^2 \cdot \text{Dif1}$ is the best detector with the potential of isolating open floods areas from grassland floods and distinguish these from nonflood areas. This detector enabled us to retrieve more information about the scattering mechanisms changes between two dates. On the other hand, it was established that the proposed model detectors Mon1 and Mon$U1$ and existing model from OPRatio Rat2 are the best at mapping flooded areas in general. The analysis was limited to areas of short vegetation only due to the nature of Sentinel-1 C band data which has minimal dense canopy penetration. This study nonetheless provides interesting and useful outputs which could be tested in densely vegetated areas and thick canopy with the availability of data with longer wavelengths and deeper penetration.

References

[1] IPCC, "Sections," in *Climate Change 2023: Synthesis Report. Contribution of Working Groups I., II, and III to the Sixth Assessment Report of the Intergovernmental Panel on Climate Change*, C. W. Team, H. Lee, and J. Romero, Eds. Geneva, Switzerland: IPCC, 2023, pp. 35–115, doi: 10.59327/IPCC/AR6-9789291691647.00334-48.

[2] E. Bieri and J. J. L. Rowley, "Too much of a good thing? Flooding poses a hidden threat to frogs on a wildfire-prone continent," *Biol. Conservation*, vol. 313, 2026, Art. no. 111550. [Online]. Available: https://www.sciencedirect.com/science/article/pii/S0006320725005877

[3] D. Ahmad and M. Afzal, "Climate change flood risks and post-flood agricultural and non-agricultural economic losses in flood-prone bait households Muzaffargarh district of Punjab, Pakistan," *Environ., Develop. Sustainability*, vol. 27, no. 8, pp. 18275–18311, 2025, doi: 10.1007/s10668-024-04674-7.

[4] L. Chen et al., "Influence of flood events on the ecological characteristics of Bolboschoenus planiculmis: Implications for restoration of Grus leucogeranus Habitats," *Water*, vol. 16, no. 24, 2024, Art. no. 3672. [Online]. Available: https://www.mdpi.com/2073-4441/16/24/3672

[5] S. Treby, S. P. Grover, and P. E. Carnell, "Impacts of fire and flooding on sediment carbon storage in a large, forested floodplain," *Environ. Conservation*, vol. 51, no. 4, pp. 270–279, 2024. [Online]. Available: https://www.cambridge.org/core/product/367984FD678DAF61662B996A08F1F8C6

[6] C. Chaudhuri, D. Braun, E. Hodgson, and C. Robertson, "Quantifying flood-pulse dynamics and associated wetland habitats for juvenile salmon in a large free-flowing river," *Sci. Total Environ.*, vol. 1009, 2025, Art. no. 181038. [Online]. Available: https://www.sciencedirect.com/science/article/pii/S0048969725026786

[7] A. Hardy, G. Oakes, and G. Ettritch, "Tropical wetland (TropWet) mapping tool: The automatic detection of open and vegetated waterbodies in Google Earth engine for tropical wetlands," *Remote Sens.*, vol. 12, 2020, Art. no. 1182.

[8] G. Lefebvre et al., "Introducing WIW for detecting the presence of water in wetlands with landsat and sentinel satellites," *Remote Sens.*, vol. 11, 2019, Art. no. 2210. [Online]. Available: https://www.mdpi.com/2072-4292/11/19/2210

[9] V. L. Inman and M. B. Lyons, "Automated inundation mapping over large areas using Landsat data and Google Earth Engine," *Remote Sens.*, vol. 12, 2020, Art. no. 1348. [Online]. Available: https://www.mdpi.com/2072-4292/12/8/1348

[10] G. Kulk et al., "Using multi-spectral remote sensing for flood mapping: A case study in Lake Vembanad, India," *Remote Sens.*, vol. 15, 2023, Art. no. 5139. [Online]. Available: https://www.mdpi.com/2072-4292/15/21/5139

[11] X. Na, S. Zang, Y. Zhang, and L. Liu, "Wetland mapping and flood extent monitoring using optical and radar remotely sensed data and ancillary topographical data in the Zhalong National Natural Reserve, China," *Proc. SPIE*, vol. 8893, 2013, Art. no. 88931M, doi: 10.1117/12.2029117.

[12] B. Slagter, N.-E. Tsendbazar, A. Vollrath, and J. Reiche, "Mapping wetland characteristics using temporally dense Sentinel-1 and Sentinel-2 data: A case study in the St. Lucia wetlands, South Africa," *Int. J. Appl. Earth Observ. Geoinf.*, vol. 86, 2020, Art. no. 102009. [Online]. Available: https://www.sciencedirect.com/science/article/pii/S0303243419307573

[13] G. A. Kordelas, I. Manakos, D. Aragonés, R. Dıáz-Delgado, and J. Bustamante, "Fast and automatic data-driven thresholding for inundation mapping with Sentinel-2 data," *Remote Sens.*, vol. 10, 2018, Art. no. 910. [Online]. Available: https://www.mdpi.com/2072-4292/10/6/910

[14] J. Ruiz-Ramos, A. Marino, A. Berardi, A. Hardy, and M. Simpson, "Characterization of natural wetlands with cumulative sums of polarimetric SAR timeseries," in *Proc. IEEE Int. Geosci. Remote Sens. Symp.*, 2021, pp. 5899–5902.

[15] M. Mleczko and M. Mróz, "Wetland mapping using SAR data from the Sentinel-1A and TanDEM-X missions: A comparative study in the Biebrza floodplain (Poland)," *Remote Sens.*, vol. 10, 2018, Art. no. 78. [Online]. Available: https://www.mdpi.com/2072-4292/10/1/78

[16] T. McCormack, J. Campanyà, and O. Naughton, "Reconstructing flood level timeseries at seasonal wetlands in Ireland using Sentinel-1," *Remote Sens. Environ.*, vol. 299, 2023, Art. no. 113839. [Online]. Available: https://www.sciencedirect.com/science/article/pii/S0034425723003905

[17] F. Canisius, B. Brisco, K. Murnaghan, M. V. D. Kooij, and E. Keizer, "SAR backscatter and InSAR coherence for monitoring wetland extent, flood pulse and vegetation: A study of the Amazon lowland," *Remote Sens.*, vol. 11, 2019, Art. no. 720. [Online]. Available: https://www.mdpi.com/2072-4292/11/6/720

[18] F. K. Isundwa et al., "Optimizing change detection methods for flood mapping using polarimetric SAR," *IEEE J. Sel. Topics Appl. Earth Observ. Remote Sens.*, vol. 18, pp. 29450–29463, 2025.

[19] B. Zhang, S. Wdowinski, D. Gann, S.-H. Hong, and J. Sah, "Spatiotemporal variations of wetland backscatter: The role of water depth and vegetation characteristics in Sentinel-1 dual-polarization SAR observations," *Remote Sens. Environ.*, vol. 270, 2022, Art. no. 112864. [Online]. Available: https://www.sciencedirect.com/science/article/pii/S0034425721005848

[20] B. Brisco et al., "Evaluation of C-band SAR for identification of flooded vegetation in emergency response products," *Can. J. Remote Sens.*, vol. 45, pp. 73–87, 2019, doi: 10.1080/07038992.2019.1612236.

[21] T. L. Evans, M. Costa, K. Telmer, and T. S. F. Silva, "Using ALOS/PALSAR and RADARSAT-2 to map land cover and seasonal inundation in the Brazilian Pantanal," *IEEE J. Sel. Topics Appl. Earth Observ. Remote Sens.*, vol. 3, no. 4, pp. 560–575, Dec. 2010.

[22] A. S. Arnesen et al., "Monitoring flood extent in the lower Amazon River floodplain using ALOS/PALSAR ScanSAR images," *Remote Sens. Environ.*, vol. 130, pp. 51–61, 2013. [Online]. Available: https://www.sciencedirect.com/science/article/pii/S0034425712004257

[23] H. Li, Z. Xu, Y. Zhou, X. He, and M. He, "Flood monitoring using Sentinel-1 SAR for agricultural disaster assessment in Poyang Lake region," *Remote Sens.*, vol. 15, 2023, Art. no. 5247. [Online]. Available: https://www.mdpi.com/2072-4292/15/21/5247

[24] M. T. Islam and Q. Meng, "An exploratory study of Sentinel-1 SAR for rapid urban flood mapping on Google Earth engine," *Int. J. Appl. Earth Observ. Geoinf.*, vol. 113, 2022, Art. no. 103002. [Online]. Available: https://www.sciencedirect.com/science/article/pii/S1569843222001911

[25] M. Billah, A. K. M. S. Islam, W. B. Mamoon, and M. R. Rahman, "Random forest classifications for landuse mapping to assess rapid flood damage using Sentinel-1 and Sentinel-2 data," *Remote Sens. Appl.: Soc. Environ.*, vol. 30, 2023, Art. no. 100947. [Online]. Available: https://www.sciencedirect.com/science/article/pii/S2352938523000290

[26] S. Plank, M. Jüssi, S. Martinis, and A. Twele, "Mapping of flooded vegetation by means of polarimetric Sentinel-1 and ALOS-2/PALSAR-2 imagery," *Int. J. Remote Sens.*, vol. 38, pp. 3831–3850, 2017, doi: 10.1080/01431161.2017.1306143.

[27] A. Marino and M. Nannini, "Signal models for changes in polarimetric SAR data," *IEEE Trans. Geosci. Remote Sens.*, vol. 60, 2022, Art. no. 5212818.

[28] A. Marino and I. Hajnsek, "A change detector based on an optimization with polarimetric SAR imagery," *IEEE Trans. Geosci. Remote Sens.*, vol. 52, no. 8, pp. 4781–4798, Aug. 2014.

[29] L. S. de Souza, J. W. Armbruster, and D. C. Werneke, "The influence of the Rupununi portal on distribution of freshwater fish in the Rupununi district, Guyana," *Cybium.*, vol. 36, no. 1, pp. 31–43, 2012.

[30] S. K. Hamilton, S. J. Sippel, and J. M. Melack, "Comparison of inundation patterns among major South American floodplains," *J. Geophys. Res.: Atmos.*, vol. 107, no. D20, pp. LBA 5–1–LBA 5–14, Oct. 2002, doi: 10.1029/2000JD000306.

[31] G. Sarmiento, "The savannas of tropical America," in *Ecosystems of the World XIII: Tropical Savannas*, F. Bourliìere, Ed. Amsterdam, The Netherlands: Elsevier, 1983, pp. 245–288.

[32] J. Beard, "The savanna vegetation of northern tropical America," *Ecol. Monographs*, vol. 23, no. 2, pp. 149–215, 1953.

[33] R. Piantanida, G. Hajduch, and J. Poullaouec, "Sentinel-1 level 1 detailed algorithm definition," ESA, Paris, France, Tech. Rep. SEN-TN-52-7445, 2016.

[34] A. Berardi, "North Rupununi Orthomosaic_B12_12 02 2020," The Open University, 2020, doi: 10.21954/ou.rd.12497711.v1.

[35] A. Berardi, "North Rupununi Orthomosaic_A1_12 02 2020," The Open University, 2020, doi: 10.21954/ou.rd.12490862.v2.

[36] A. Berardi, "North Rupununi Orthomosaic_P1_08 02 2020," The Open University, 2020, doi: 10.21954/ou.rd.12452384.v1.

[37] A. Berardi, "North Rupununi Orthomosaic_P2_11 02 2020," The Open University, 2020, doi: 10.21954/ou.rd.12452387.v1.

[38] A. Berardi, "North Rupununi Orthomosaic_P3_16 02 2020," The Open University, 2020, doi: 10.21954/ou.rd.12452390.v1.

[39] A. Berardi, "North Rupununi Orthomosaic_P4_18 02 2020," The Open University, 2020, doi: 10.21954/ou.rd.12452393.v1.

[40] A. Berardi, "North Rupununi Orthomosaic_P6_13 02 2020," The Open University, 2020, doi: 10.21954/ou.rd.12453221.v1.

[41] A. Berardi, "North Rupununi Orthomosaic_P7_13 02 2020," The Open University, 2020, doi: 10.21954/ou.rd.12453248.v1.

[42] A. Berardi, "North Rupununi Orthomosaic_P5_16 02 2020," The Open University, 2020, doi: 10.21954/ou.rd.12452396.v1.

[43] S. R. Cloude and E. Pottier, "A review of target decomposition theorems in radar polarimetry," *IEEE Trans. Geosci. Remote Sens.*, vol. 34, no. 2, pp. 498–518, Mar. 1996.

[44] S. R. Cloude and E. Pottier, "An entropy based classification scheme for land applications of polarimetric SAR," *IEEE Trans. Geosci. Remote Sens.*, vol. 35, no. 1, pp. 68–78, Jan. 1997.

[45] C. López-Martínez and E. Pottier, *Basic Principles of SAR Polarimetry*. Cham, Switzerland: Springer, 2021.

[46] A. Verma, A. Bhattacharya, and S. Dey, "Scattering power components from dual-pol SLC and GRD SAR data," in *Proc. 8th Asia-Pacific Conf. Synthetic Aperture Radar*, 2023, pp. 1–4.

[47] C. Lopez-Martinez, E. Pottier, and S. R. Cloude, "Statistical assessment of eigenvector-based target decomposition theorems in radar polarimetry," *IEEE Trans. Geosci. Remote Sens.*, vol. 43, no. 9, pp. 2058–2074, Sep. 2005.

[48] J. M. Lopez-Sanchez, F. Vicente-Guijalba, J. D. Ballester-Berman, and S. R. Cloude, "Polarimetric response of rice fields at C-band: Analysis and phenology retrieval," *IEEE Trans. Geosci. Remote Sens.*, vol. 52, no. 5, pp. 2977–2993, May 2014.

[49] I. H. Woodhouse, *Introduction to Microwave Remote Sensing*. Boca Raton, FL, USA: CRC Press, 2017.



Felix Kasiti Isundwa (Member, IEEE) received the B.Sc. degree in Earth sciences (hydrology and water resources management option) from Maseno University, Maseno, Kenya, in 2013, and the M.Sc. degree in water policy from the Institute of Water and Energy Sciences, Pan African University, Tlemcen, Algeria, in 2018. He is currently working toward the Ph.D. degree in mapping and monitoring floods using SAR polarimetry with the Faculty of Natural Sciences, University of Stirling, Stirling, U.K.

From 2014 to 2016, he was a Consulting Hydrologist. In 2019, he joined SERVIR Eastern and Southern Africa project with the Regional Centre for Mapping of Resources for Development, Nairobi, Kenya, as an Assistant Hydrologist.



Armando Marino (Member, IEEE) received the M.Sc. degree in telecommunication engineering from Universita' di Napoli "Federico II", Naples, Italy, in 2006, and the Ph.D. degree in polarimetric SAR interferometry from the School of Geosciences, University of Edinburgh, Edinburgh, U.K. in 2011.

In 2006, he joined the High Frequency and Radar Systems Department, German Aerospace Centre, Oberpfaffenhofen, Germany, where he developed his M.Sc. thesis. From March 2011 to October 2011, he was with Institute of Computing Research, University of Alicante, Barcelona, Spain. From December 2011 to May 2015, he was a Postdoctoral Researcher and Lecturer with ETH Zurich, Institute of Environmental Engineering, Zürich, Switzerland. From June 2015, he was a Lecturer with the School of Engineering and Innovation, Open University, Milton Keynes, U.K. Since May 2018, he has been an Associate Professor with the Faculty of Natural Sciences, University of Stirling, Stirling, U.K.



Andrea Berardi received the B.Sc. (Hons) degree in ecology from King's College, University of London, London, U.K., in 1992, the M.Sc. degree in conservation from University College London, London, in 1994, the Ph.D. degree in geography/conservation from the University of London, in 1999, and the Certificate of Higher Education in charity and social enterprise management from Anglia Ruskin University, Chelmsford, U.K., in 2013.

He is currently an Educator and Researcher inspired by systems thinking to apply holistic, accessible, visual, and participatory methodologies to support communities and decision-makers in working through complex local challenges. He is also a Part-time Senior Lecturer in environmental information systems with The Open University, Milton Keynes, U.K., and a Co-Director of the Cobra Collective CIC, Egham, U.K., a social enterprise, which uses different knowledge systems, accessible technologies and creative art approaches to engage marginalized communities worldwide in self-determination. His research interests includes facilitating grassroots approaches to ecological sustainability and social justice through place-based training, education programmes, and research.



C Isabella Bovolo received the B.Sc. (Hons.) degree in geochemistry from the University of Manchester, Manchester, U.K., in 1995, and the Ph.D. degree in computational thermodynamics from the Department of Earth Sciences, University of Bristol, Bristol, U.K., in 2002.

She was a Postdoctoral Researcher with the Water Resources Group, School of Engineering, Newcastle University, Newcastle upon Tyne, U.K. She then became a Resident Scientist with the Iwokrama International Centre for Rainforest Conservation and Development, Georgetown, Guyana, where she established a hydrological monitoring system and conducted other research. She was a Consultant Hydrologist for the World Bank on a range of international flood risk management projects. In 2016, she became an Assistant Professor of physical geography with Durham University, Durham, U.K. Her research interests include hydrology, climate modeling and monitoring, the quantification of physical processes, and combines the study of these processes with an understanding of the role of people in managing their environments.



Peter Hunter received the B.Sc. (Hons.) degree in environmental science and the Ph.D. degree in Earth observation from the University of Stirling, Stirling, U.K., in 2003 and 2007, respectively.

From 2007 to 2024, he held a range of research and academic positions with the University of Stirling, contributing extensively to the development of new technologies and approaches for environmental monitoring and modeling. In August 2024, he became a Professor of the digital environment with the University of Stirling, where he is also the Science Director of Forth-ERA Digital Environmental Observatory. He is currently an Environmental Scientist. His research interests include the integration of data from Earth observation, wireless sensor networks and models to improve the monitoring, and understanding and management of ecosystems.



Claire Neil received the First Class B.Sc. (Hons.) degree in physics from the University of Strathclyde, Glasgow, Scotland, U.K., in 2007, and the Ph.D. degree in Physics from the University of Strathclyde in 2011.

He is currently a Principal Scientist with the Scottish Environment Protection Agency, Stirling, U.K., where she leads the development of SEPA's Earth Observation capabilities. She has 18 years of experience in Earth observation, and her expertise includes optical modelling, radiative transfer physics, image and signal processing, and algorithm development. Her research focuses on enabling U.K. regulators to fully exploit the advantages that Earth observation can offer for comprehensive environmental monitoring.

Dr. Neil was the recipient of the NERC Knowledge Exchange Fellowship based at the University of Stirling, in 2016, with the aim of developing satellite remote sensing as an operational data resource for water managers across the U.K.



Thiago S. F. Silva received the B.Sc. degree in biology from the University of Rio Grande do Norte, Natal, Brazil, in 2002, the M.Sc. degree in remote sensing from the National Institute for Space Research (INPE), São Paulo, Brazil, in 2004, and the Ph.D. degree in physical geography from the University of Victoria, Victoria, BC, Canada, in 2009.

In 2010, he was a Researcher with the University of California Santa Barbara, Santa Barbara, CA, USA, and INPE from 2011 to 2013. From 2013 to 2019, he was an Assistant Professor with the Geography Department, São Paulo State University, São Paulo. Since 2019, he has been a Senior Lecturer with the Faculty of Natural Sciences, University of Stirling, Stirling, U.K. His research interests include ecology, geoscience, and data science to understand how global ecosystems are being affected by the global climatic and biodiversity crises.